Cellular electrical micro-impedance parameter artifacts produced by passive and active current regulation

[1]Anthony E. English and [2]James C. Squire

[1]The University of Tennessee,

Department of Mechanical, Aerospace and Biomedical Engineering,

Knoxville, TN 37996 USA

[2]Virginia Military Institute, Department of Electrical and Computer Engineering,

Lexington, Virginia 24450

Running title: Cellular electrical micro-impedance artifacts

Address correspondence to:

Anthony E. English

Tel: (865) 974-8392

Fax: (865) 974-7663

Email: tenglish@utk.edu

Abstract

This study analyzes the cellular microelectrode voltage measurement errors produced by active and passive current regulation, and the propagation of these errors into cellular barrier function parameter estimates. The propagation of random and systematic errors into these parameters is accounted for within a Riemannian manifold framework consistent with information geometry. As a result, the full non-linearity of the model parameter state dependence, time dependent instrumental noise distributions, and systematic errors associated with the voltage to impedance conversion, are accounted for. Specifically, cellular model parameters are treated as the coordinates of a model space manifold that inherits a Riemannian metric from the data space. The model space metric is defined in terms of the pull back of an instrumental noise dependent Fisher information metric. Additional noise sources produced by the evaluation of the cell covered electrode model function that is a function of a naked electrode random variable are also included in the analysis. Based on a circular cellular micro-impedance model in widespread use, this study shows that coaxial cable capacitances and circuit loading can significantly alter the sensitivity of the parameter estimates. The results of this study further show that impedance systematic errors can produce significant and highly model state dependent parameter deviations.

Keywords—Biomedical transducers; biological cell; endothelial, impedance; information geometry; measurement errors; parameter estimation

I. INTRODUCTION

Micro-impedance sensors have applications ranging from toxicology screening to cellular motility and adhesion interaction studies. One of the most common micro-impedance sensors currently available consists of a gold microelectrode with a large counter electrode.[15, 16] Although these sensors have become increasingly used to probe and study time and frequency dependent cellular impedances,[1, 4, 7-9, 12, 19, 21-24, 26, 28-30] several forms of random and systematic error can potentially corrupt these impedance measurements. Despite the importance of this technology, few studies have made any attempt to identify and reduce these errors and their propagation into parameter estimates of cellular barrier function and attachment.[31]

Several forms of time and frequency dependent artifacts can potentially corrupt cellular micro-impedance measurements.[11] Systems based on phase sensitive detection are particularly susceptible to synchronous and 60 Hz noise. Following phase sensitive detection[20] this noise can appear at different frequencies depending on the lock-in frequency. The sampling rate can also produce complicated noise components as a result of aliasing. Gaussian noise exists in most circuits and even with very efficient filtering, analog to digital noise is always present and sets a lower limit to the achievable resolution.

In practice, the microelectrode impedance is estimated by measuring the voltage across the microelectrode while applying an approximately constant 1μA current through it. Current sources consisting of a 1MΩ resistor placed in series with a 1V source and the electrode are relatively common. This configuration provides an approximately constant

1μA current source assuming the electrode impedance is much less than 1MΩ. The large frequency dependent changes in the gold electrode impedance, however, can potentially introduce frequency dependent loading artifacts. Furthermore, coaxial cable capacitances can distort the impedance estimate if they are not accounted for and the current is assumed a constant 1μA. Even if an active current source is used, loading and capacitances can produce systematic errors in this system.

The nonlinearity of the functions used to model cellular barrier function are coupled to both time dependent and systematic instrumental noise and present a significant obstacle to cellular barrier function analysis. The sensitivity of each of the parameters can vary significantly from one model state to another.[5] A recent study has quantifying this sensitivity with respect to instrumental noise fluctuations using information geometry.[10] Geometric methods can account for both systematic and random error propagation. Random error propagation can be accounted for by transformations of the Fisher metric while systematic errors can be accounted for by the geodesic shift distances in the parameter values from their true values based on the Fisher metric.

The objective of this study is to quantify the time dependent and systematic error propagation into cellular impedance parameter estimates using both passive and active current sources. Using a consistent geometric framework, a data space metric is defined in terms of time dependent instrumental noise levels and model states are mapped into this data space. Systematic errors are quantified by calculating the geodesic distance between displaced parameter states that arise from the voltage to impedance conversion.

II. METHODS AND MATERIALS

To meet this study's objective, impedance estimates of a cell covered industry standard gold microelectrode and an electrode circuit model, with known impedance, will be obtained using two circuit configurations. One circuit configuration, commonly implemented in these types of measurements, uses a large resistor in series with the electrode to give an approximately constant 1μA current source. The other circuit uses a transconductance amplifier to provide a more constant 1μA current source. Using an electrode circuit model with a known impedance, within an error defined by the component resistor and capacitor tolerances, the voltage to impedance conversion models are tested. This system's random and systematic errors are then used to define a data metric for a parameter precision and geodesic displacement analysis. The cell covered electrode model, instrumental circuit configuration and noise levels are unified within a consistent Riemannian manifold framework of information geometry.

A. Cell Culture

Endothelial cells were isolated from porcine pulmonary arteries obtained from a local abattoir. The endothelial cells were cultivated at 37 ^{o}C and 5% CO_2. Cell culture media consisted of M199 (GibcoBRL) and 10% fetal bovine serum (Hyclone) supplemented with vitamins (Sigma), glutamine (GibcoBRL), penicillin and streptomycin (GibcoBRL), and amino acids (Sigma). Endothelial cells were inoculated onto a series of gold

microelectrodes (Applied Biophysics) coated with fibronectin (BD Biosciences) to facilitate cellular adhesion.

B. Cellular Impedance Circuit Electronics and Analysis

A lock-in amplifier (Stanford Research SR830) provided 1 volt AC reference signals between 10Hz and 100kHz to the electrode via either a series 1MΩ resistor or a voltage controlled Howland pump current source as shown in Figs. 1a and 1b. In the first configuration, shown in Fig. 1, a 1MΩ resistor was used in series with the $1v_{rms}$ AC reference signal. In the second configuration, shown in Fig. 1b, a voltage controlled current source maintained a constant 1μA current.

Figure 2 shows a detailed schematic of the active current source shown in Fig. 1b. The voltage-dependent current source is constructed using a modified Howland current pump with a precision FET input high common mode rejection ratio operational amplifier to produce a transimpedance amplifier with an extremely high output impedance [17]. If the resistors are perfectly matched the output impedance using an AD845 operational amplifier is over 500MΩ; this degrades to 25MΩ when using 0.1% resistors, a twenty-five fold improvement over using a passive current source. The circuit is composed of an inverting amplifier U1 connected to a modified Howland current pump U2. The inverting amplifier reduces the signal amplitude by a factor of 100, corrects the signal phase inversion introduced by the second stage inverting Howland current pump, and provides the ability to adjust the transconductance gain, via R3, and correct for any small

voltage offset, via R11, that would otherwise cause a small DC bias current to flow through the electrode array.

Using basic circuit analysis,[18] the measured electrode voltage based on the passive current source shown in Fig. 1a is

$$v_e(z_e) = \left\{ \frac{z_L(z_e)}{z_{cc} + z_L(z_e) + z_s + \frac{z_s}{z_{ps}} z_{cc} + \frac{z_s}{z_{ps}} z_L(z_e)} \right\} v_s , \tag{1}$$

where v_e the measured electrode voltage, z_e represents either the naked, cell covered or electrode model impedance, $z_{ps} = 1/j\omega C_{ps}$, $z_{pc} = 1/j\omega C_{pc}$ and $z_{pv} = 1/j\omega C_{pv}$ represent coaxial lead impedances, $R_s = 50\Omega$ the current source impedance, $R_{cc} = 1\text{M}\Omega$, $z_v = R_v/(1 + j\omega R_v C_v)$ the lock in amplifier input impedance and the term

$$z_L(z_e) = \frac{z_{pc} z z_{pv} z_v}{z_e z_{pv} z_v + z_{pc} z_{pv} z_v + z_{pc} z_e z_v + z_{pc} z_e z_{pv}} , \tag{2}$$

represents the parallel combination of the circuit elements to the right of R_{cc}. When the source resistance, $z_s = R_s$, is very small compared to z_{ps}, this result simplifies to the familiar voltage divider law, i.e.,

$$v_e(z_e) = \left\{ \frac{z_L(z_e)}{z_{cc} + z_L(z_e)} \right\} v_s . \tag{3}$$

Converting the measured voltage to an equivalent impedance therefore follows from the inverse relation

$$z_e(z_e) = \frac{z_v \left(z_{cc} + z_s + \frac{z_s}{z_{ps}} z_{cc} \right)}{z_v \left(\frac{v_s}{v_e} - 1 - \frac{z_s}{z_{ps}} \right) - \left(\frac{z_v}{z_{pc}} + \frac{z_v}{z_{pv}} + 1 \right) \left(z_{cc} + z_s + \frac{z_s}{z_{ps}} z_{cc} \right)} . \tag{4}$$

In the limit that the source voltage resistance, R_s, is small

$$z_e \left(\frac{v_e}{i} \right) = \frac{z_v z_{cc}}{z_v \left(\frac{v_s}{v_e} - 1 \right) - \left(\frac{z_v}{z_{pc}} + \frac{z_v}{z_{pv}} + 1 \right) z_{cc}} . \tag{5}$$

If, in addition, the lock-in amplifier input impedance, Z_v, is very large

$$z_e \left(\frac{v_e}{i} \right) = \frac{z_{cc}}{\left(\frac{v_s}{v_e} - 1 \right) - \left(\frac{1}{z_{pc}} + \frac{1}{z_{pv}} \right) z_{cc}} . \tag{6}$$

Notice the inverted parallel combination of z_{pc} and z_{pv}. In the limit that the parallel combination of z_{pc} and z_{pv} is very large

$$z_e \left(\frac{v_e}{i} \right) = \frac{z_{cc}}{\left(\frac{v_s}{v_e} - 1 \right)} \qquad \text{or} \qquad z_e = \frac{z_{cc} v_e}{v_s - v_e} \tag{7}$$

When z_{cc} is much smaller than the z_c then $v_e << v_s$ we get

$$z_e \left(\frac{v_e}{i} \right) = \frac{v_e z_{cc}}{v_s} \tag{8}$$

The measured voltage using the constant current source shown in Fig. 1b is

$$v_e \left(\frac{v_e}{i} \right) = \frac{1}{\frac{1}{z_e} + \frac{1}{z_{pa}} + \frac{1}{z_{pc}} + \frac{1}{z_{pv}} + \frac{1}{z_v}} i \tag{9}$$

where z_c is the electrode impedance, $z_{pa} = 1/\{j\omega C_{pa}\}$, $z_{pc} = 1/\{j\omega C_{pc}\}$, and $z_{pv} = 1/\{j\omega C_{pv}\}$, represent coaxial lead impedances, and $z_v = R_v/(1 + j\omega R_v C_v)$ the lock-in amplifier impedance. The corresponding impedance, given the measured voltage is

$$z_e \left(\frac{v_e}{i} \right) = \frac{1}{\frac{1}{v_e} i - \left(\frac{1}{z_{pa}} + \frac{1}{z_{pc}} + \frac{1}{z_{pv}} + \frac{1}{z_v} \right)} \tag{10}$$

In the limit that the lock-in amplifier input impedance is very large, the cell covered impedance reduces to

$$z_e(\omega) = \frac{1}{\frac{1}{v_e} i - \left(\frac{1}{z_{pa}} + \frac{1}{z_{pc}} + \frac{1}{z_{pv}} \right)} \tag{11}$$

Furthermore, if the coaxial cable capacitance are small, then

$$z_e(\omega) = \frac{v_e}{i_s} \tag{12}$$

C. Electrode model and calibration

Figure 3 shows the electrode circuit model used to evaluate the system.[27] This circuit provides a known frequency dependent impedance standard, within the propagated tolerance of the circuit components, to evaluate the system. The component values were chosen to produce a similar voltage response to the naked electrode over the frequency range of interest. The circuit model impedance, z_{mod}, is

$$z_{\text{mod}} = \frac{R_p}{1 + j\omega R_p C_p} + R_c, \tag{13}$$

where R_p, C_p, and R_c are the resistive and capacitive elements defined in the circuit shown in Fig. 3. A BK Precision 889A Bench LCR/ESR Meter also provided coaxial cable, electrode circuit model, and cellular microelectrode impedances measurements.

D. Cell covered electrode model

Figure 4 outlines a quantitative description of an endothelial cell monolayer layer cultivated on an electrode. Current can flow between cells, underneath the cells and through the membrane via capacitive and resistive coupling. Given the above system, the following question needs to be addressed. Which combination of parameters can be successfully optimized for a given level of instrumental noise and what circuit parameters produce the most relevant systematic errors in this system?

A closed form solution for circular cells base on the continuity arguments outlined in Fig. 4 have been derived in previous studies,[13, 14] and is given by

$$\psi = Z_n \left[\frac{Z_n}{Z_n + Z_m} + \frac{\dfrac{Z_m}{Z_n + Z_m}}{\dfrac{\gamma r_c}{2} \dfrac{I_0(\gamma r_c)}{I_1(\gamma r_c)} + R_b \left(\dfrac{1}{Z_n} + \dfrac{1}{Z_m} \right)} \right]^{-1}, \tag{14}$$

where Z_c is the cell covered electrode impedance, Z_n the naked electrode impedance, Z_m the cell membrane impedance, R_b the cell-cell junction impedance, r_c is the radius of a single cell, and $I_0(\gamma r_c)$ and $I_1(\gamma r_c)$ are modified Bessel functions of the first kind of zero and first order, respectively. The variable γ is defined as

$$\gamma = \sqrt{\frac{\rho}{h} \left(\frac{1}{Z_n} + \frac{1}{Z_m} \right)}. \tag{15}$$

where ρ is the media resistivity and h is the cell substrate separation distance. The cell membrane impedance, Z_m, can be considered a series combination of apical and basal membrane impedance that consists of a parallel resistor and capacitor combinations, i.e.,

$$Z_m = \frac{2R_m}{1 + j2\pi f R_m C_m}, \tag{16}$$

where each membrane consists of a parallel resistor, R_m, and capacitor, Cm, combination.

A parameter, α, can be defined as

$$\alpha = r_c \sqrt{\frac{\rho}{h}} . \tag{17}$$

that represents the cell-matrix impedance.

Based the model given by Eq. 14, this study will consider the two parameters α and R_b, to be optimize based on voltage measurements, are treated as the local coordinates of a model space and the impedance function, Z_c, maps these points into an impedance data space.

E. Riemannian Manifold

The measurement of each physical impedance state $\zeta \in Z$ produces a statistical distribution of measured voltages depending on the experimental configuration, ρ, defined by the circuit parameters and the instrumental data acquisition settings. If C represents the space of all experimental configurations, such that $\rho \in C$, then define the map, $h : Z \times C \to S : \zeta \times \rho \mapsto p(\cdot, \theta)$ from the physical space Z to a manifold, $S = \{p(v, \theta) : \theta = \{\theta^1, ..., \theta^n\} \in \Theta\}$ [2, 3] of measured voltages. The term v represents a random voltage variable belonging to the sample space $V = \Re^{2n}$ and $p(v, \theta)$ is the probability density function of v, parameterized by θ. The experimental configuration or control space, $C \subset \Re^m$, is parameterized by the set of variables c having components that represent the circuit element variables, C_{pv}, R_{cc}, R_v, etc., illustrated in Fig. 1. The mapping $h(\zeta, \rho)$ from the measurement state (ζ, ρ) to the population probability distribution, $p(v, \theta)$ defines the errors associated with a given measurements. The mean

and variance of $p(v, \theta)$ can be used to define the systematic and random errors associated with a particular measurement. In practice, statistical estimators of the mean and variance can be applied to actual measurements and used in the analysis.

The subscripts n and c will be used to denote the naked electrode or cell covered electrode cases. For example, the measurement of the naked electrode impedance, $Z_{n,}$ and the cell covered impedance, Z_c, have associated spaces S_n and S_c, respectively. A similar convention will applied to the other spaces, maps and points. Since the same circuit configuration is used to make both naked and cell covered electrode measurements, the same set of control parameters define the maps $g_n(\zeta, \rho)$ and $g_c(\zeta, \rho)$.

The set of parameters $m = (\alpha, R_b)$ represent the cellular model space coordinates of some open subset M of Euclidean space. The fact that the naked electrode impedance must be included in the domain of the model function introduces an additional complication in the analysis. The cellular impedance model function given by Eq. 14, ψ: $M \times Z_n \rightarrow Z_c \subset \Re^{2n}$, maps each model state $\varepsilon \in M$ and naked electrode impedance state, $\zeta_n \in Z_n$, into a cell covered impedance physical space element, $\zeta_c \in Z_c \subset \Re^{2n}$. The two sets of 2n coordinate components, $z_n = (z_n^{\,1}, ..., z_n^{\,2n})$ and $z_c = (z_c^{\,1}, ..., z_c^{\,2n})$, of the naked and cell covered electrode physical spaces, Z_n and Z_c, respectively, represent the real and imaginary parts of the n frequencies $\{f_1, .., f_n\}$.

There exist two forms or error associated with the optimization of model states using cell micro-impedance measurements. The first arises because measurements of a particular cell covered impedance state produce a distribution of measured voltages governed by the population probability density $p_c(x_c, \theta_c)$. The second arises because naked electrode impedance estimates are required to evaluate the model state mapping

$\psi: M \times Z_n \rightarrow Z_c \subset \Re^{2n}$. The mapping $g^{-1}: S_n \times C_n \rightarrow Z_n$, therefore, implies that z_n is a random variable as is z_c under the transformation ψ. This contribution can be consider as the probability density $p_n(x_n, \theta_n(g_n \cdot \psi^{-1}))$ as a function of the cell covered impedance state z_c. Hence, when both the naked and cell covered noise distributions are considered the sample space can be defined as $X = X_n \times X_c$, where X_n is the sample space for the naked electrode random variable, x_n, and X_c is the cell covered sample space for the cell covered random variable x_c. The joint distribution on X is $p(x,\theta)$. If the probabilities are independent, then $p(x,\theta) = p_n(x_n,\theta_n) \cdot p_c(x_c,\theta_c)$. Although a probability density $p_n(x_n, \theta_n(g_n \cdot \psi^{-1}))$ as a function of the cell covered impedance state z_c, it is more convenient to include this contribution using push forwards and pull backs of an equivalent metric to be defined shortly.

For the purpose of this study, we will assume that each physical impedance value, z, produces a normal distribution of voltage values when it is measured. The manifold S, therefore, consists of all normal probability distribution functions on the sample space $X = \Re^{2n}$ parameterized by a single coordinate chart (Θ, θ) consisting of the components of the mean μ and the components of the upper triangle Δ of the population covariance matrix Σ, i.e.,

$$p(x, \mu, \Sigma) = (2\pi \det \Sigma)^{-n} \exp\left(-\frac{1}{2}(x-\mu)^T \Sigma (x-\mu)\right), \qquad (18)$$

where T is the transpose, and the coordinate chart maps $p(x, \theta)$ to the ordered pair (μ, Δ) in $\Re^{2n} \times \Re^{2n \times n+n}$. Associated with each set of parameters $z = (z^1, z^2, \ldots z^{2n})$ is a mean, μ, and population covariance matrix $\Sigma(z)$ that are assumed to vary smoothly with respect to

z. Accuracy is related to the mapping from z into μ and precision is related to the mapping from z into Σ.

We may define the composite smooth functions $h_c = g_c \cdot \psi_\cdot : M \to S_c$ by

$$h_c(\mu) = p(\cdot, \pi) \quad g_c(\psi(\tau_1, \ldots, \tau_n)) \quad g_c(\psi(\tau_{n+1}, \ldots, \tau_{n(n+3)/2})) \tag{19}$$

Similarly, the composite smooth functions $h_n = g_n \cdot \psi^{-1} \cdot \psi_\cdot : M \to S_n$ by

$$h_n(\tau) = p(\cdot, \pi) \quad g_n(\psi(\tau_1, \ldots, \tau_n)) \quad g_c(\psi(\tau_{n+1}, \ldots, \tau_{n(n+3)/2})) \tag{20}$$

The composite maps, h_c and h_n, therefore assigns to each set of model state π the normal distributions such that the mean and covariance matrix are associated with π, both of which may be estimated by experimental data. Assuming that the functions h_n and h_c are regular (i.e. the differentials g_{n*} and g_{c*}. of the composite maps, $\psi = \phi \cdot Z_c$, has maximal rank), the image $D = \psi(M)$ of M in S is a (possibly immersed) submanifold of S. As such it locally satisfies the definition of a statistical manifold [2, 3]. Note that it follows from basic differential geometry that if the function $y \to \mu(Z_c(y))$ is regular then ψ will also be regular. Likewise, if μ is one-to-one then ψ will also be and by definition D will be an embedded manifold and not immersed.

The Fisher metric on the manifold S is defined as

$$g_{ab}(\theta) = E\left[\frac{\partial}{\partial\theta^a}\ln p(\cdot;\theta)\frac{\partial}{\partial\theta^b}\ln p(\cdot;\theta)\right] \tag{21}$$

where E denotes the expectation value and the indices $1 \le a,b \le 2n$. In the case of a normal distribution, the Fisher information matrix becomes

$$g_{ab} = \frac{\partial \boldsymbol{\mu}^T}{\partial z^a}\Sigma^{-1}\frac{\partial \boldsymbol{\mu}}{\partial z^b} + \frac{1}{2}tr\left(\Sigma^{-1}\frac{\partial \Sigma}{\partial z^a}\Sigma^{-1}\frac{\partial \Sigma}{\partial z^b}\right) \tag{22}$$

$$\frac{\partial \boldsymbol{\mu}^T}{\partial z^a} = \left\{ \frac{\partial \mu^1}{\partial z^a}, \frac{\partial \mu^2}{\partial z^a}, \ldots \frac{\partial \mu^{2n}}{\partial z^a} \right\} \tag{23}$$

$$\frac{\partial \Sigma}{\partial z^a} = \begin{bmatrix} \frac{\partial \Sigma^{1,1}}{\partial z^a} & \frac{\partial \Sigma^{1,2}}{\partial z^a} & \cdots & \frac{\partial \Sigma^{1,2n}}{\partial z^a} \\ \frac{\partial \Sigma^{2,1}}{\partial z^a} & \frac{\partial \Sigma^{2,2}}{\partial z^a} & \cdots & \frac{\partial \Sigma^{2,2n}}{\partial z^a} \\ \vdots & \vdots & \ddots & \vdots \\ \frac{\partial \Sigma^{2n,1}}{\partial z^a} & \frac{\partial \Sigma^{2n,2}}{\partial z^a} & \cdots & \frac{\partial \Sigma^{2n,2n}}{\partial z^a} \end{bmatrix} \tag{24}$$

If the covariance matrix, Σ, does not vary significantly with respect to change in the data state, we can use the fact that

$$g_{ab} = \frac{\partial \boldsymbol{\mu}^T}{\partial z^a} \Sigma^{-1} \frac{\partial \boldsymbol{\mu}}{\partial z^b} = \Sigma^{-1}_{ab} \tag{25}$$

to greatly simplify the analysis.

F. Precision Analysis

Two important contributions to the parameter uncertainty need to be considered. First, for a given naked electrode impedance state, $\zeta_n \in Z_n$, each model state, $\varepsilon \in M$ is mapped into a cell covered impedance state, $\zeta_c \in Z_c$, such that $\psi : M \times Z_n \to Z_c : \varepsilon \times \zeta_n \mapsto \zeta_c$ that has an associated statistical distribution, $p_c(x_c, \theta_c)$, via the experimental configuration map $h_c : Z_c \times C_c \to S_c : \zeta_c \times \rho_c \mapsto p_c \left(\zeta_c, \theta_c \right)$ of measured cell covered voltage states. The pull back of the Fisher metric associated with the measured cell covered voltage noise distribution sets an upper bound on the attainable precision produced by this noise source. The second, and subtler, contribution arises because naked electrode impedance estimates, z_n, are required to evaluate the model

function. The transformation, or push forward, of the naked electrode error distribution to the cell covered electrode impedance value must therefore also be included. These two sources of error can be included by evaluating the push forward of the model function map $\psi : M \times Z_n \to Z_c$, i.e.,

$$D\psi = \begin{bmatrix} D_m\psi & D_{z_n}\psi \end{bmatrix} = \begin{bmatrix} \frac{\partial z_c}{\partial m} & \frac{\partial z_c}{\partial z_n} \end{bmatrix} \tag{26}$$

where

$$D_m\psi = \frac{\partial z_c}{\partial m} = \begin{bmatrix} \frac{\partial z_c^1}{\partial \alpha} & \frac{\partial z_c^1}{\partial R_b} & \frac{\partial z_c^1}{\partial C_m} & \frac{\partial z_c^1}{\partial R_m} \\ \frac{\partial z_c^2}{\partial \alpha} & \frac{\partial z_c^2}{\partial R_b} & \frac{\partial z_c^2}{\partial C_m} & \frac{\partial z_c^2}{\partial R_m} \\ \vdots & \vdots & \vdots & \vdots \\ \frac{\partial z_c^{2k}}{\partial \alpha} & \frac{\partial z_c^{2k}}{\partial R_b} & \frac{\partial z_c^{2k}}{\partial C_m} & \frac{\partial z_c^{2k}}{\partial R_m} \end{bmatrix} \text{ and} \tag{27}$$

$$D_{z_n}\psi = \frac{\partial z_c}{\partial z_n} = \begin{bmatrix} \frac{\partial z_c^1}{\partial z_n^1} & \frac{\partial z_c^1}{\partial z_n^2} & \cdots & \frac{\partial z_c^1}{\partial z_n^{2n}} \\ \frac{\partial z_c^2}{\partial z_n^1} & \frac{\partial z_c^2}{\partial z_n^2} & \cdots & \frac{\partial z_c^2}{\partial z_n^{2n}} \\ \vdots & \vdots & \ddots & \vdots \\ \frac{\partial z_c^{2k}}{\partial z_n^1} & \frac{\partial z_c^{2k}}{\partial z_n^2} & \cdots & \frac{\partial z_c^{2k}}{\partial z_n^{2k}} \end{bmatrix}. \tag{28}$$

Similarly, the push forward of the cell covered electrode impedance to cell covered electrode voltage map, $h_c : Z_c \times C_n \to S_c$, is given by

$$Dh_c = \begin{bmatrix} D_{z_c}h_c & D_{c_c}h_c \end{bmatrix} = \begin{bmatrix} \frac{\partial v_c}{\partial z_c} & \frac{\partial v_c}{\partial c_c} \end{bmatrix} \tag{29}$$

and the push forward of the naked electrode impedance to naked electrode voltage map, $h_n : Z_n \times C_n \to S_n$, is given by

$$Dh_n = \begin{bmatrix} D_{z_n} h_n & D_{c_n} h_n \end{bmatrix} = \begin{bmatrix} \frac{\partial v_n}{\partial z_n} & \frac{\partial v_n}{\partial c_n} \end{bmatrix} \tag{30}$$

The pull back of the cell covered noise Fisher metric gives rise to the model space metric G_c defined as

$$\begin{aligned} G_c\left(\frac{\partial}{\partial m^a} \quad \frac{\partial}{\partial m^b}\right) &= g_{S_c}\left(D_{z_c} h_c \cdot \psi, g_{S_c}\right) \\ &= g_{S_c}\left(D_{z_c} h_c \cdot D_m \psi \frac{\partial}{\partial m^a} \quad D_{z_c} h_c \cdot D_m \psi \frac{\partial}{\partial m^b}\right), \end{aligned} \tag{31}$$

while the pull back of the naked electrode noise contribution, G_n, is

$$\begin{aligned} G_n\left(\frac{\partial}{\partial m^a} \quad \frac{\partial}{\partial m^b}\right) = \\ g_{S_n}\left(D_{z_n} h_n \cdot D_{z_n} \psi^{-1} \cdot D_m \psi \frac{\partial}{\partial m^a} \quad Dz_n h_n \cdot D_{z_n} \psi^{-1} \cdot D_m \psi \frac{\partial}{\partial m^b}\right) \end{aligned} \tag{32}$$

An additional complication that needs to be addressed is the propagation of errors in the circuit element values used to convert the measured voltages into impedances. The measurement and electrode circuit model component values have uncertainties given by the manufacturer's specifications and/or the multi-meter precision. To ensure that these errors are not contributing significantly to the parameter precision analysis, a Fisher matrix that embodies their assumed Gaussian errors is defined on the control spaces used to define the impedance to voltage conversion. The naked and cell covered control spaces are defined in terms of the Cartesian product $C_n = C_c = R_{cc} \times C_p$ and the electrode circuit model $C_m = R_p \times C_p \times R_c$. The naked and cell covered to impedance to voltage conversion are therefore defined as $\varphi_n : C_n \times Z_n \to V_n$ and $\varphi_c : C_c \times Z_c \to V_c$, respectively. The sensitivity to the circuit component uncertainties can be tested using the block diagonal Fisher metric defined on $C_n \times Z_n$ and $C_c \times Z_c$. To include these

contributions a similar set of pull backs are defined to describe the model parameter precision in terms of the circuit component tolerances, i.e.,

$$G_{C_c} \left(\frac{\partial}{\partial m^a} \quad \frac{\partial}{\partial m^b} \right) =$$
$$\left(D_{c_c} h_c \cdot D_m \psi \frac{\partial}{\partial m^a} \quad D_{c_c} h_c \cdot D_m \psi \frac{\partial}{\partial m^b} \right) \qquad \text{and} \qquad (33)$$

$$G_{C_n} \left(\frac{\partial}{\partial m^a} \quad \frac{\partial}{\partial m^b} \right) =$$
$$\left(D_{c_n} h_n \cdot D_{z_n} \psi^{-1} \cdot D_m \psi \frac{\partial}{\partial m^a} \quad D_{c_n} h_n \cdot D_{z_n} \psi^{-1} \cdot D_m \psi \frac{\partial}{\partial m^b} \right) \cdot \qquad (34)$$

G. Experimental Probability Estimation

To apply the above theory in practice, it is necessary to use experimental measurements to estimate the underlying, or true, distribution and propagate the errors in terms of the Fisher information metric. The Fisher metric is estimated from the measured naked and cell covered electrode noise statistics. Average voltage estimates of the population average, μ, were calculated from the N data samples, or observations, at each frequency, i.e.,

$$\bar{v}_j = \frac{1}{N} \sum_{i=1}^{N} v_j^i \qquad (35)$$

where $\bar{v}_j$ represents the data sample average at the jth frequency and v_j^i represents the ith voltage sample at the jth frequency. The data variance-covariance matrix at each frequency,

$$s_j = \begin{bmatrix} s_j^{\Re\Re} & s_j^{\Re\Im} \\ s_j^{\Im\Re} & s_j^{\Im\Im} \end{bmatrix} \tag{36}$$

is calculated using the relations

$$s_{f_k}^{\Re\Re} = \sum_{i=1}^{N} \frac{\left(v_{\Re f_k}^{i} - \bar{v}_{\Re f_k}\right)\left(v_{\Re f_k}^{i} - \bar{v}_{\Re f_k}\right)}{(N-1)}, \qquad s_{f_k}^{\Re\Im} = \sum_{i=1}^{N} \frac{\left(v_{c\Re f_k}^{i} - \bar{v}_{c\Re f_k}\right)\left(v_{c\Im f_k}^{i} - \bar{v}_{c\Im f_k}\right)}{(N-1)},$$

$$s_{f_k}^{\Im\Re} = \sum_{i=1}^{N} \frac{\left(v_{c\Im f_k}^{i} - \bar{v}_{c\Im f_k}\right)\left(v_{c\Re f_k}^{i} - \bar{v}_{c\Re f_k}\right)}{(N-1)}, \text{ and} \qquad s_{f_k}^{\Im\Im} = \sum_{i=1}^{N} \frac{\left(v_{c\Im f_k}^{i} - \bar{v}_{c\Im f_k}\right)\left(v_{c\Im f_k}^{i} - \bar{v}_{c\Im f_k}\right)}{(N-1)}, \tag{37}$$

where the real and imaginary impedance component standard deviations are defined as

$$s_j^{\Re\Re} = \sqrt{S_j^{\Re\Re}} \quad \text{and} \quad s_j^{\Im\Im} = \sqrt{S_j^{\Im\Im}}\,, \tag{38}$$

respectively. The correlation coefficient at frequency fk are calculated from the relation

$$r_j^{\Re\Im} = r_j^{\Im\Re} = \frac{s_j^{\Re\Im}}{\sqrt{s_j^{\Re\Re}}\sqrt{s_j^{\Im\Im}}}\,. \tag{39}$$

The unbiased variance-covariance matrix, s_{fk}, at frequency f_k provides an unbiased estimate of the population variance –covariance matrix Σ_{fk}.

Errors in the statistical estimators of the mean and variance of the underlying probability density also contribute to the uncertainty. The population variance of the sample mean and sample variance based on *n* samples can be used to justify ignoring this effect. The analysis presented in this study will assume that these contributions are negligible and then justify this assumption. The uncertainties in the circuit elements produce another Fisher metric on the control spaces involved in the voltage to impedance conversion.

III. RESULTS

The results of this study are organized in such a way to illustrate the different error sources and their contribution to the accuracy and precision of the cellular impedance and model parameters. Using the Fisher information matrix, random noise produces a decrease in parameter precision while systematic errors decrease the accuracy by producing displacements from the true value. Parts A and B quantify the random and systematic errors in this system and their effect on voltage measurements and impedance estimates while parts C and D illustrate the propagation of these errors into the model parameter estimates.

A. Random sample space voltage estimates

Figure 5 provides a statistical summary of the measured voltages from a naked gold electrode, a cell covered gold electrode and the electrode circuit model shown in Fig. 3. At each frequency, the statistics of 64 voltage measurements sampled at a rate of 32Hz for 2 seconds were evaluated using Eqs. 35-37. The electrode circuit model frequency dependent average voltages are in qualitative agreement with that of the gold electrode. Assuming a constant 1μA electrode current, the equivalent impedances can be estimated by scaling the measured voltages by a factor of 10^6. Figure 5 also illustrates the real and imaginary frequency dependence of the noise variance of the naked electrode, the cell covered electrode and the resistor and capacitor electrode model. At lower frequencies the resistor and capacitor model has a lower noise level than the naked and cell covered

electrodes. A variance peak, consistent with 60 Hz noise, is also present in the resistor and capacitor circuit model.

The conceptual images that one should have while reading the statistical results presented in Fig. 5 are the following. An estimate of the location of the naked, cell covered and model electrode states in their respective probability manifolds are first obtained by calculating the frequency dependent averages and covariance components. Although n different frequencies are measured, one should still think of this as a single point in a neighborhood of $\Re^{2n}\times\Re^{2nn+n}$ on the naked, S_n, cell covered, S_c, and electrode model, S_m, probability manifolds. The uncertainty associated with this point, based on the number of samples in the statistical estimator, defines neighborhoods of the naked, U_n, cell covered, U_c, probability manifolds and model U_m to examine. The number of data samples, N, in this study is assumed large enough to justify a single point of the naked electrode probability manifold with respect to the uncertainties in this system.

B. Systematic voltage data space displacements

Figure 6 shows the measured and predicted normalized and random impedance deviations of the electrode circuit model shown in Fig. 3 using the passive and active circuit configurations. Direct LCR measurements are included for comparison. In Figs. 6a and 6b, the voltage measurements for both the passive and Howland current sources were scaled by a factor of 10^6 to produce impedance estimates assuming a constant 1μA electrode current. Figures 6c and 6d show the data space components of the deviations to the ideal 1μA current source evaluated using the Fisher metric. Using the frequency

dependent noise levels shows a different pattern than the normalized data. During a numerical optimization, these will be the regions that contribute the most to systematic errors. The high frequency regions contribute significantly to the optimized fit error if they are not weighted out. It is important to realize that these quantified shifts based on the Fisher information metric are more important than the normalized curves shown in Figs. 6a and 6b. It is clear from Figs. 6c and 6d that the parasitic capacitive elements will have a more severe effect on the parameter optimization if they are not corrected.

The components of the geodesic displacement between states assuming a constant 1 μA current source and corrections produced by the circuit model show at what frequencies the most significant errors contributing to the parameter uncertainty occur since the total error or variance will be a sum of these components.

C. Model parameter precision analysis

In the absence of systematic errors, random noise fluctuations can enter into the parameter optimization though both the naked and cell covered electrode measurements. For this particular study, Fig. 5 summarizes the statistics of a representative naked and cell covered electrode that the following results will be based on. Figure 7 shows a precision analysis resulting from pulling the cell covered electrode and naked electrode noise metrics back to the model space. The top row of subplots, (a-c), summarizes a precision analysis produced by cell covered electrode fluctuations while the bottom row, (d-f) shows the contribution produced by the naked electrode. Plots (a) and (d) refer to

the parameter α while plots (b) and (e) refer to the parameter R_b. Plots (c) and (f) summarize the case when both parameters are considered simultaneously.

The α-R_b determinant component justifies the local assumption of an isomorphism. When the mapping Z_c is one-to-one it is possible to push forward a probability density, function, or vector field. It is then possible to push forward the noise probability density of the naked electrode by the function Z_c. The regularity of the function Z_c is necessary for this to be possible.

D. Systematic model space geodesic displacements

Systematic errors in the measured voltages enter into the data analysis through both the naked and the cell covered electrode impedance estimates. Figure 8 shows the weighted separation distance in the data space to the model submanifold using a passive current source and an ideal constant current source. The displacement from each submanifold model state produced by the measured coaxial capacitance Cp, Rcc, and Load impedance as a function of the model state. The displacement is equivalent to the increase in χ^2 produced by the systematic error components.

Parameter systematic errors can enter through systematic errors in either the naked, cell covered, or a combination of both the naked and cell covered electrode impedance measurements. In both the passive and active current sources, systematic errors produced by the naked electrode are less than those produced by the cell covered electrode. When both sources of systematic errors are included, the overall systematic errors are less than that produced by the cell covered electrode by itself. Some of

compensation, therefore, occurs when the naked and cell covered electrode systematic errors occur together. The systematic errors produced by the cell covered electrode dominate the overall systematic errors error. Increasing values of R_b and decreasing α values are more sensitive to naked electrode systematic errors. Increasing values of R_b and α model states are more susceptible to cell covered impedance systematic errors. In the absence of any circuit model corrections, a constant current source produces a significant reduction in systematic errors compared to the passive current source. Although an active current source reduces the systematic errors compare to the passive source, large values of χ^2 still remain for most states.

E. Random and systematic corrections to optimized model parameters

To correct the systematic errors indicated in Fig. 8 a calibration correction at each frequency point was carried out using known series resistance and capacitor combinations at each frequency. Based on the frequency dependent impedance estimates of the naked and cell covered electrode a range of capacitors and resistors were chosen at each frequency to provide a calibration of known impedances. The quoted error was based on the propagated voltage following the interpolation transformation and the calibration standard errors. Figure 9 shows the impedance estimates based on the calibration and corrections at each frequency.

IV. DISCUSSION

The quantification of cellular barrier function parameters optimized from electrical impedance measurements is complicated by the model non-linearity, frequency dependent noise levels, and systematic errors associated with the voltage to impedance conversion. Noise estimates play a critical role in optimizing and quantifying these parameters. By constructing a Fisher metric using measured noise levels, it is possible to examine the contributions of naked and cell covered electrode measurements to the parameter precision. Systematic errors can be quantified as the geodesic separation distances evaluated using the Fisher metric. Noise measurements also play an important role in stabilizing the parameter analysis. If noise measurements are not included in the optimization, the data rarely converges to meaningful results. The large errors that occur at low frequencies produce instabilities in the optimization if these data points are equally weighted with the rest of the data.

Random and time dependent noise reduce the attainable parameter precision. Complications in the error propagation arise because some of the parameters in the maps are themselves random variables. The fact that the naked electrode impedance must be input to the model function introduces an additional noise source in the analysis. The model function maps model states into the data space. These data space points make up a submanfold of the data space. Each of these points in turn maps to a probability function that represents the propagation of the naked electrode impedance. The separation

distance between this distribution and that representing an experimental measurement can be defined.

The systematic error produced by uncorrected loading from Rcc, coaxial capacitances Cp, and lock-in amplifier impedance has two important effects on the parameter optimization. Systematic errors shift the measured voltage away from the true voltage and thereby increase the chi squared value for this model state. The maximum likelihood point can also be shifted to another model state. This assumes the model is correct in the first place. Systematic errors, however, limited this minimum separation distance as indicated by the large χ^2 values.

Increasing random noise levels decrease the model state precision. In this sensor and model, however, systematic errors have a much more detrimental effect on the parameter estimates if they are not corrected. Relatively small amounts of parasitic capacitances produce large shifts in the location of the model state. This study also partially explains the very large χ_ν^2 values observed in previous studies. In particular, coaxial cable capacitances can produce large shift in the impedance value.

The statistical approximation to the population covariance-variance matrix will introduce an error into the Fisher information matrix that will translate into parameter precision limits. The question is how many data points are required so that this contribution is negligible? Propagating the numerical precision back onto the model space may also be considered in some cases with model functions that have very large precision ranges.

The number of data samples was assumed large enough to justify taking the estimated states as a single point. In reality, the finite sampling of data points introduces another

source of uncertainty in the system. The Cramer-Rao theorem[2, 25] states that the covariance of any unbiased estimator $\hat{\theta} = (\hat{\theta}^i)$ is bounded by the inverse of the Fisher information matrix, i.e.,

$$Cov(\hat{\theta}^i, \hat{\theta}^j) \geq g^{ij} \tag{40}$$

where $a^{ij} \geq b^{ij}$ implies that $a^{ij} - b^{ij}$ forms a positive semi-definite matrix. This limit is attained asymptotically in the sense that if $\hat{\theta}_N$ is an estimator based on the N independent observation $x^1, x^2, \ldots, x^N$ from the distribution $p(x, \theta)$, then the covariance of $\hat{\theta}_N$ tends to g^{ij} / N as N tends to infinity,

$$Cov(\hat{\theta}^i, \hat{\theta}^j) \rightarrow \frac{1}{N} g^{ij} \tag{41}$$

The distribution of the estimator $\hat{\theta}_N$ tends to the normal distribution $N(\theta, g^{ij} / N)$.

Active current regulation corrects for the effect of increasing electrode impedance. Active current regulation, however, does overcome the loading effects of capacitive coupling at higher frequencies. At higher frequencies the noise levels are relatively smaller than those at lower frequencies for a given set of filter settings. The use of an active current source . Carefully circuit model corrections in converting the measured voltage into an equivalent impedance were necessary in both cases.

When used with a lock-in amplifier a Howland current source significantly reduced systematic errors associated with impedance estimates below 1 kHz compared to a passive current source. At frequencies above 1 kHz, however, both the passive and active current source configurations produced significant errors. Direct measurements with an LCR meter suggest that a lock-in amplifier configuration is the source of these errors.

Normalized plots of the resistance and reactance are problematic for a number of reasons when trying to quantify electrical impedance data. The correct propagation of errors in this data would be as follows. Given the tolerances, or errors, associated with each element, ΔR_p, ΔC_p, and ΔR_c, the errors in the real and imaginary parts of the impedance are propagated[6] based on Eq 13 using the relations

$$\Delta R_{\mathrm{mod}}^2 = \left(\frac{1-\omega R_p C_p^2}{1+\omega R_p C_p^2} \right)^2 \Delta R_p^2 + \left(\frac{-2\omega^2 R_p^3 C_p}{1+\omega R_p C_p^2} \right)^2 \Delta C_p^2 + \Delta R_c^2 , \tag{42}$$

and

$$\Delta X_{\mathrm{mod}}^2 = \left(\frac{-2\omega R_p C_p}{1+\omega R_p C_p^2} \right)^2 \Delta R_p^2 + \left(\frac{-\omega R_p^2 \left(-\omega^2 R_p^2 C_p^2\right)}{1+\omega R_p C_p^2} \right)^2 \Delta C_p^2 . \tag{43}$$

Comparing measurements to an LCR meter also has be done with caution. Since the LCR meter provided impedance measurements as magnitude and phase information, the meter tolerance errors were propagated using the relations

$$\Delta R_{LCR} = \sqrt{\cos\theta_{LCR}\Delta Z_{LCR}^2 + Z_{LCR}^2 \sin\theta_{LCR}\Delta\theta_{LCR}^2} , \tag{44}$$

$$\Delta X_{LCR} = \sqrt{\sin\theta_{LCR}\Delta Z_{LCR}^2 + Z_{LCR}^2 \cos\theta_{LCR}\Delta\theta_{LCR}^2} , \tag{45}$$

The normalized deviation of the measured resistances and reactances from the known values follows from the relations

$$R_{nm} = \left\langle R_{\mathrm{exp}} \right\rangle - R_{\mathrm{mod}} / R_{\mathrm{mod}} \tag{46}$$

and

$$X_{nm} = \left\langle X_{\exp} \right\rangle - X_{\mathrm{mod}} \Big/ X_{\mathrm{mod}}, \tag{47}$$

Respectively, where $\langle R_{\exp} \rangle$ represents the experimentally estimated average resistance, $\langle X_{\exp} \rangle$ the experimentally estimated average reactance, R_{mod} the known model resistive component of z_{mod}, and X_{mod} the known model reactive component of z_{mod}. The errors associated with the normalized resistance and reactance are approximated using a propagation of errors based on the relations

$$\Delta R_{nm} = \sqrt{\left(\frac{-R_{\exp}}{R_{\mathrm{mod}}^2} \right)^2 \left(\Delta R_{\exp} \right)^2 + \left(\frac{1}{R_{\mathrm{mod}}} \right)^2 \left(\Delta R_{\mathrm{mod}} \right)^2} \text{ and} \tag{48}$$

$$\Delta X_{nm} = \sqrt{\left(\frac{-X_{\exp}}{X_{\mathrm{mod}}^2} \right)^2 \left(\Delta X_{\exp} \right)^2 + \left(\frac{1}{X_{\mathrm{mod}}} \right)^2 \left(\Delta X_{\mathrm{mod}} \right)^2}, \tag{49}$$

where $(\Delta R_{\exp})^2$ represents the experimentally estimated real variance, $(\Delta X_{\exp})^2$ represents the experimentally estimated imaginary variance, $(\Delta R_{\mathrm{mod}})$ is given by Eq. 42 and $(\Delta X_{\mathrm{mod}})^2$ is given by Eq. 43.

V. CONCLUSION

The evaluation of cellular barrier function parameters based on electrical impedance measurements in this study were most significantly affected by systematic errors rather than precision limitations. That is, the accuracy was far less than the precision in most cases. Systematic errors therefore produce the most significant contribution to the optimized parameter χ^2 values. Time dependent and systematic errors entered into the

parameter uncertainty via both the naked and cell covered electrode measurements. The fact that circuit corrections for the systematic errors did not lower the reduced chi squared, χ_ν^2, value to approximately unity indicates that other factors, such as the model or other errors, are contributing to the fit.

ACKNOWLEDGMENT

Grant support from the National Science Foundation in the form of a CAREER award, grant number BES-0238905 (AE), and the American Heart Association, grant number 0265029B (AE), is gratefully acknowledged.

REFERENCES

[1]Aas, V., S. Torbla, M.H. Andersen, J. Jensen, and A.C. Rustan. Electrical stimulation improves insulin responses in a human skeletal muscle cell model of hyperglycemia. *Ann. N.Y. Acad. Sci.* 967:506-515, 2002.

[2]Amari, S.-c., Differential-geometric methods in statistics. Springer-Verlag, New York. 1985.

[3]Amari, S.-i. and H. Nagaoka, Methods of information geometry. Oxford University Press, Oxford. 2000.

[4]Antony, A.B., R.S. Tepper, and K.A. Mohammed. Cockroach extract antigen increases bronchial airway epithelial permeability. *J. Allergy Clin. Immunol.* 110:589-595, 2002.

[5]Beck, J.V. and K.J. Arnold, Parameter estimation in engineering and science. John Wiley & Sons, New York. 1977.

[6]Bevington, P.R., Data reduction and error analysis for the physical sciences. McGraw-Hill, New York. 1969.

[7]Burns, A.R., R.A. Bowden, S.D. MacDonell, D.C. Walker, T.O. Odebunmi, E.M. Donnachie, S.I. Simon, M.L. Entman, and C.W. Smith. Analysis of tight junctions during neutrophil transendothelial migration. *Journal of Cell Science* 113:45-57, 2000.

[8]Burns, A.R., D.C. Walker, E.S. Brown, L.T. Thurmon, R.A. Bowden, C.R. Keese, S.I. Simon, M.L. Entman, and C.W. Smith. Neutrophil transendothelial migration is independent of tight junctions and occurs preferentially at tricellular corners. *J. Immunol.* 159:2893-2903, 1997.

[9]Ellis, C.A., C. Tiruppathi, R. Sandoval, W.D. Niles, and A.B. Malik. Time course of recovery of endothelial cell surface thrombin receptor (par-1) expression. *Am. J. Physiol. (Cell Physiol.)* 276:C38-C45, 1999.

[10]English, A.E., C.P. Plaut, and A.B. Moy. A riemannian manifold analysis of endothelial cell monolayer impedance parameter precision. *Journal of Mathematical Biology* (In Press):2007.

[11]English, A.E., J.C. Squire, J.E. Bodmer, and A.B. Moy. Endothelial cell electrical impedance parameter artifacts produced by a gold electrode and phase sensitive detection. *IEEE Trans. Biomed. Eng.* 54:(In Press), 2007.

[12]Gainor, J.P., C.A. Morton, J.T. Roberts, P.A. Vincent, and F.L. Minnear. Platelet-conditioned medium increases endothelial electrical resistance independently of camp/pka and cgmp/pkg. *Am. J. Physiol. Heart Circ. Physiol.* 281:H1992-H2001, 2001.

[13]Giaever, I. and C.R. Keese. Correction: Micromotion of mammalian cells measured electrically. *Proc. Natl. Acad. Sci. USA* 90:1634, 1993.

[14]Giaever, I. and C.R. Keese. Micromotion of mammalian cells measured electrically. *Proc. Natl. Acad. Sci. USA* 88:7896-7900, 1991.

[15]Giaever, I. and C.R. Keese. Monitoring fibroblast behavior in tissue culture with an applied electric field. *Proc. Natl. Acad. Sci. USA* 81:3761-3764, 1984.

[16]Giaever, I. and C.R. Keese. Use of electric fields to monitor the dynamical aspect of cell behavior in tissue culture. *IEEE Trans. Biomed. Eng.* BME-33:242-247, 1986.

[17]Horowitz, P. and W. Hill, The art of electronics. Cambridge University Press, Cambridge, United Kingdom. 1989.

[18]Irwin, D.J. and Chwan-Hwa, Basic engineering circuit analysis, New York. 1990.

[19]Kataoka, N., K. Iwaki, K. Hashimoto, S. Mochizuki, Y. Ogasawara, M. Sato, K. Tsujioka, and F. Kajiya. Measurements of endothelial cell-to-cell and cell-to-substrate gaps and micromechanical properties of endothelial cells during monocyte adhesion. *Proc. Natl. Acad. Sci.* 99:15638-15643, 2002.

[20]Meade, M.L., Lock-in amplifiers: Principles and applications. Peter Peregrinus / IEE, London. 1983.

[21]Moy, A.B., K. Blackwell, N. Wang, K. Haxhinasto, M.K. Kasiske, J. Bodmer, G. Reyes, and A. English. Phorbol ester-mediated pulmonary artery endothelial barrier dysfunction through regulation of actin cytoskeletal mechanics. *Am. J. Physiol. Lung Cell Mol. Physiol.* 287:L153-L167, 2004.

[22]Moy, A.B., B. Scott, S. Shasby, and D.M. Shasby. The effect of histamine and cyclic adenosine monophosphate on myosin light chain phophorlylation in human umbilical vein endothelial cells. *J. Clin. Invest.* 92:1198-1206, 1993.

[23]Moy, A.B., J. VanEngelenhoven, J. Bodmer, J. Kamath, C. Keese, I. Giaver, S. Shasby, and D.M. Shasby. Histamine and thrombin modulate endothelial focal adhesion through centripetal and centrifugal forces. *J. Clin. Invest.* 97:1020-1027, 1996.

[24]Moy, A.B., M. Winter, A. Kamath, K. Blackwell, G. Reyes, I. Giaever, C. Keese, and D.M. Shasby. Histamine alters endothelial barrier function at cell-cell and cell-matrix sites. *Am. J. Physiol. Lung. Cell Mol. Physiol.* 278:L888-L898, 2000.

[25]Rao, C.R. Information and accuracy attainable in the estimation of statistical parameters. *Bull. Calcutta. Math. Soc.* 37:81-91, 1945.

[26]Tiruppathi, C., A.B. Malik, P.J.D. Vecchio, C.R. Keese, and I. Giaever. Electrical method for detection of endothelial cell shape change in real time: Assessment of endothelial barrier function. *Proc. Natl. Acad. Sci. USA* 89:7919-7923, 1992.

[27]Webster, J.G., ed. *Medical instrumentation: Application and design*. Third ed., John Wiley & Sons, Inc.: New York. 691. 1998

[28]Wegener, J., C.R. Keese, and I. Giaever. Electric cell-substrate impedance sensing (ecis) as a noninvasive means to monitor the kinetics of cell spreading to artificial surfaces. *Exp. Cell Res.* 259:158-166, 2000.

[29]Wegener, J., C.R. Keese, and I. Giaever. Recovery of adherent cells after in situ electroporation monitored electrically. *BioTechniques* 33:348-357, 2002.

[30]Wegener, J., M. Sieber, and H.-J. Galla. Impedance analysis of epithelial and endothelial cell monolayers cultured on gold surfaces. *J. Biochem. Biophys. Methods* 32:151-170, 1996.

[31]Xiao, C., B. Lachance, G. Sunahara, and J.H.T. Luong. An in-depth analysis of electric cell-substrate impedance sensing to study the attachment and spreading of mammalian cells. *Anal. Chem.* 74:1333-1339, 2002.

FIGURE CAPTIONS

Figure 1 Passive and active circuit configurations for cellular impedance measurements. The circuit parameters in both cases are: $V_{AC} = 1 \angle 0^o$, $R_s = 50\ \Omega$, $C_{ps} = 86$ pF, $R_{cc} = 1$ MΩ, $C_{pv} = 90$ pF, $R_v = 10$ MΩ, and $C_v = 25$ pF. (a) In the passive current source configuration, a large 1 MΩ resistor, R_{cc}, provides an approximately constant current provided that it is much greater than the electrode load impedance Z_e. The parasitic capacitance of the coaxial cable connecting R_s to R_{cc} produces a negligible contribution as a result of the low source impedance. (b) In the active current source configuration, a voltage to current source converter provides an almost constant 1 μA current source to the remainder of the circuit.

Fig. 2 Constant 1 μA current source based on a Howland pump. A precision field effect transistor with a high common mode rejection ratio operational amplifier produces a transimpedance amplifier with an extremely high output impedance. The inverting amplifier U1 connects to a modified Howland current pump U2. The inverting amplifier reduces the signal amplitude by a factor of 100 and corrects the signal phase inversion introduced by the second stage inverting Howland current pump. The inverting amplifier also provides the ability to adjust the transconductance gain, via R3, and corrects for any small voltage offset, via R11.

Figure 3 Two electrode gold electrode circuit model. The manufacturer's labeled values were $R_p = 1.00 \pm 0.01$ MΩ, $C_p = 10.0 \pm 0.2$ nF, and $R_c = 2.20 \pm 0.02$ kΩ. The measured values using a BK Precision 889A Bench LCR/ESR Meter were $R_p = 0.975 \pm 0.001$ MΩ, $C_p = 8.656 \pm 0.001$ nF, and $R_c = 2.165 \pm 0.001$ kΩ.

Figure 4 Model system definition. (a) The total measured impedance is a function of the naked electrode resistance, Z_n, the impedance underneath the cells, α, the trans-cellular impedance, Z_m, and the resistance between adjacent cell, R_b. (b) A micro-continuum description of the cell covered electrode can be formulated by defining the basal, I, electrode, I_n, and membrane, I_m, currents as a function or the radial coordinate r. The electrode voltage is V_n and the surrounding electrolyte has a voltage V_0.

Figure 5 Circuit model, naked electrode and cell covered electrode voltage statistics as a function of frequency using the passive current source. (a) The real noise variances of the cell covered, $<\Re_c^2>$, and naked, $<\Re_n^2>$, electrodes are similar but the circuit model, $<\Re_m^2>$, is significantly less at lower frequencies. (b) The imaginary cell covered, $<\Im_c^2>$, naked, $<\Im_n^2>$, and model, $<\Im_m^2>$, variance components show a similar pattern to the real variance measurements. (c) The average values of the cell covered, $<\Re_c>$, naked, $<\Re_n>$, and circuit model, $<\Re_m>$, resistive mean components decrease with increasing frequency and are in qualitative agreement with each other. (d) The average reactive components of the cell covered, $<\Im_c>$, naked, $<\Im_n>$, and circuit model, $<\Im_m>$, components show a similar pattern to the real values. The electrode circuit model noise levels are significantly lower than the electrode noise levels at lower frequencies.

Figure 6 The normalized and statistical systematic deviations of frequency dependent real and imaginary impedance components. (a) The normalized deviation of the resistance, $(R_c - R_n)/R_n$, following a 10^6 scaling shows the voltage divider effect that occurs at low frequencies when a passive current source is used and a constant 1μA electrode current is assumed. Using an active current source partially corrects this. (b) The normalized reactance shows a similar voltage divider effect at low frequencies and large normalized deviations at high frequencies produced by circuit capacitances and other artifacts. (c) The geodesic displacements of the real impedance shows the significance of the circuit capacitive effects at higher frequencies. Although the normalized deviations show the voltage divider effects, the circuit capacitive elements produce statistically more significant at higher frequencies. Using a constant current source does not correct this. (d) A similar increasing geodesic separation distance is observed at increasing frequencies with the imaginary impedance component.

Figure 7 Parameter precision analysis of α, R_b and joint α-R_b using the Fisher metric induced when naked electrode covered fluctuations (a-c) or naked electrode fluctuations (d-f) are used to define the Fisher metric. Plots (a) and (d) refer to the parameter α while plots (b) and (e) refer to the parameter R_b. Plots (c) and (f) summarize the case when both parameters are considered simultaneously.

Figure 8 Systematic errors produced by naked and cell covered impedance estimates using a passive and constant current source. (a-c) Passive systematic errors. Plot (a) shows the systematic errors produced by the naked electrode only, (b) the cell covered electrode and (c) both naked and cell covered electrode impedance systematic errors. (d-f) Constant current systematic error summary shows the systematic errors produced by the (d) naked electrode, (e) cell covered, and (f) combination of both naked and cell covered electrode errors. A constant current source significantly reduces the systematic errors. The cell covered systematic errors make a more significant contribution to the systematic errors. The combination of naked and cell covered systematic errors partially compensate each other.

Figure 9 Last showing improved data fit with optimized curve. The three model fits illustrate the case of (a) including random noise without any systematic error corrections, (b) including both random and systematic errors in the optimization. Not including any noise measurements in the optimization produces very poor quality fits that often do not converge to meaningful results. Including noise measurements stabilizes the convergence but still produces poor quality fits ($\chi_v^2 = 8.417\times10^6$). Including systematic errors significantly improves the quality of the fit ($\chi_v^2 = 9.889 \times 10^5$).

FIGURE 1

(a) Passive current source

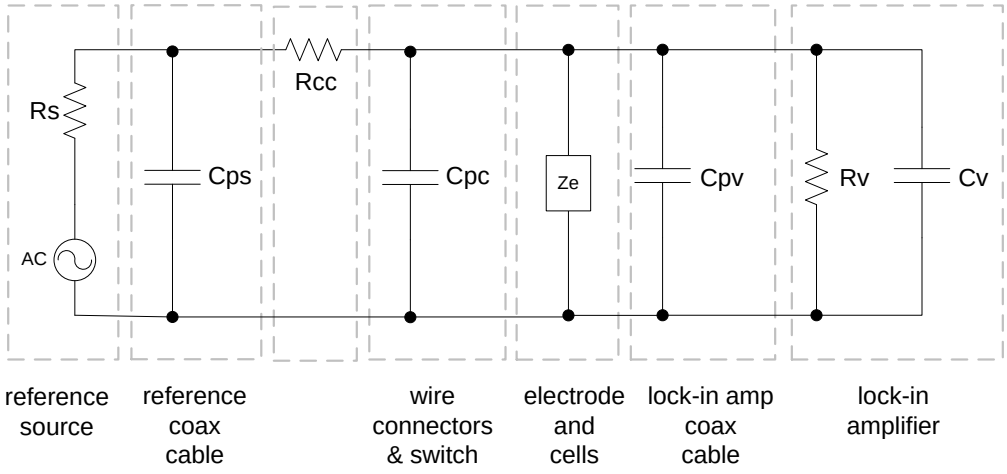

(b) Active current source

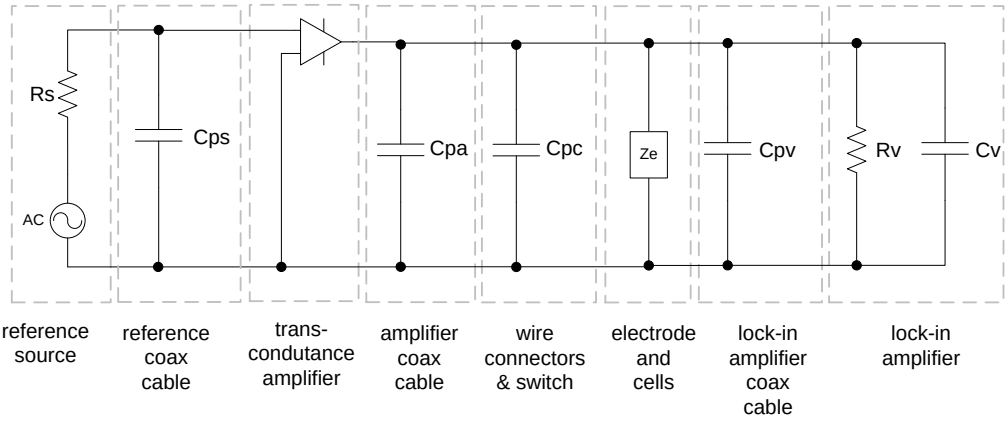

FIGURE 2

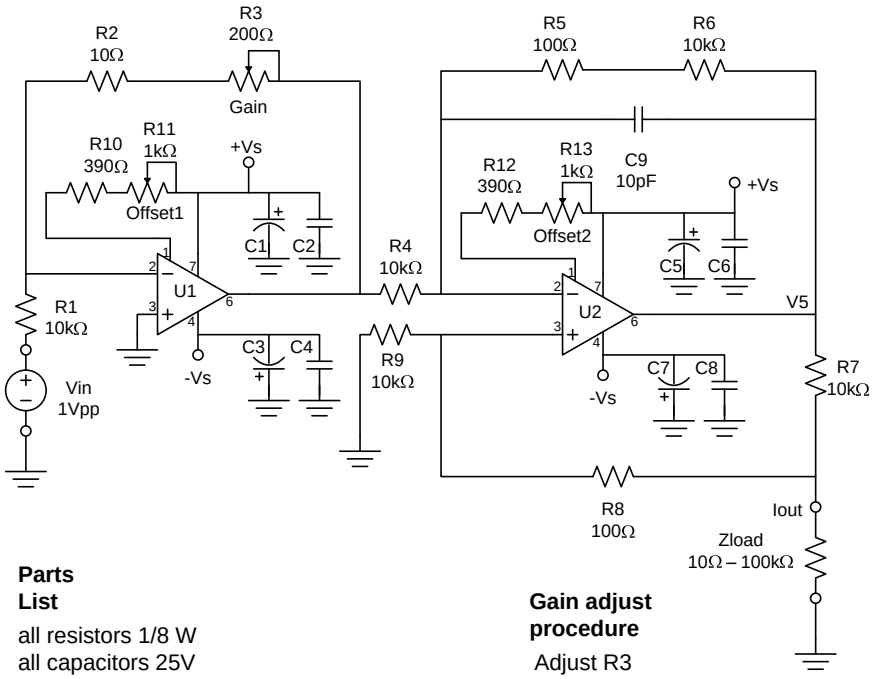

Parts List

all resistors 1/8 W
all capacitors 25V

U1,2	AD845 16MHz precision opamp
C1,3,5,7	4.7μF tantalum
C2,4,6,8	0.1μF ceramic
C9	10pF ceramic
R1	10kΩ, 1%
R2	10Ω, 5%
R3	200Ω, 1 turn potentiometer
R4,6,7,9	10kΩ, 0.1%
R5,8	100Ω, 0.1%
R10,12	390Ω, 5%
R11,13	1kΩ, 10 turn potentiometer

Gain adjust procedure

Adjust R3
0Ω gives 0.1μA/V
100Ω gives 1μA/V
200Ω gives 2μA/V

Offset adjust procedure

adjust R11 and R13 in any combination to remove DC bias in Vout

FIGURE 3

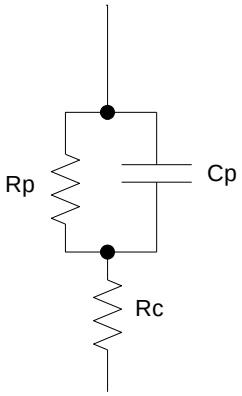

FIGURE 4

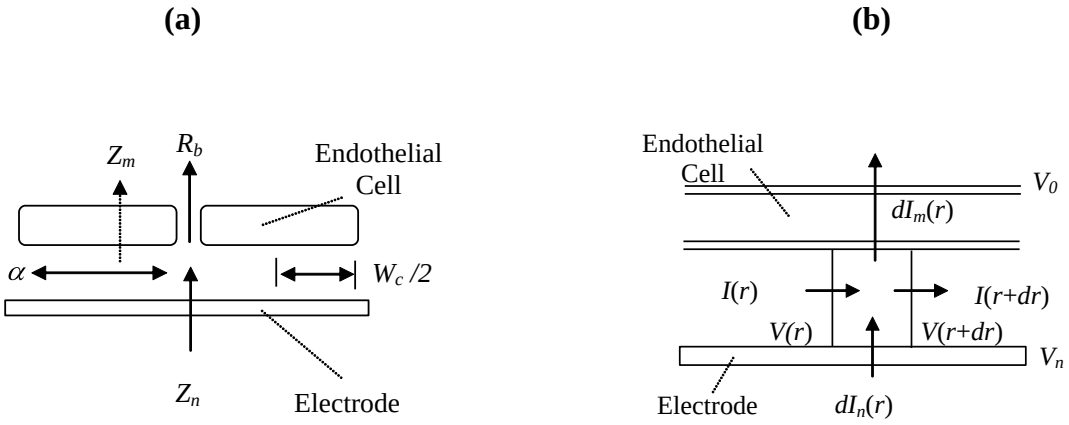
(a)
(b)
Z_m
R_b
Endothelial Cell
α
W_c /2
Z_n
Electrode
Endothelial Cell
V_0
$dI_m(r)$
$I(r)$
$I(r+dr)$
$V(r)$
$V(r+dr)$
V_n
Electrode
$dI_n(r)$

FIGURE 5

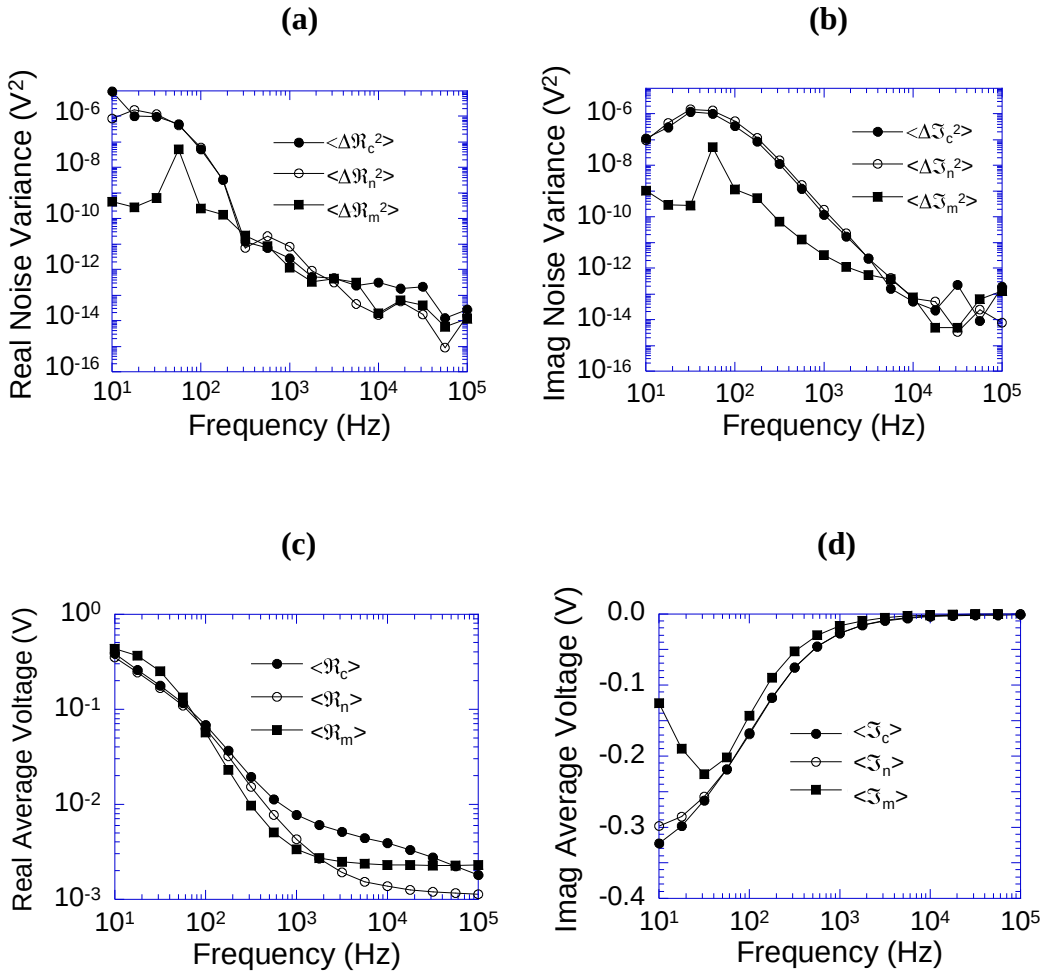
(a)
(b)
(c)
(d)
Real Noise Variance (V²)
Imag Noise Variance (V²)
Real Average Voltage (V)
Imag Average Voltage (V)
Frequency (Hz)
<Δℜc²>
<Δℜn²>
<Δℜm²>
<Δℑc²>
<Δℑn²>
<Δℑm²>
<ℜc>
<ℜn>
<ℜm>
<ℑc>
<ℑn>
<ℑm>

FIGURE 6

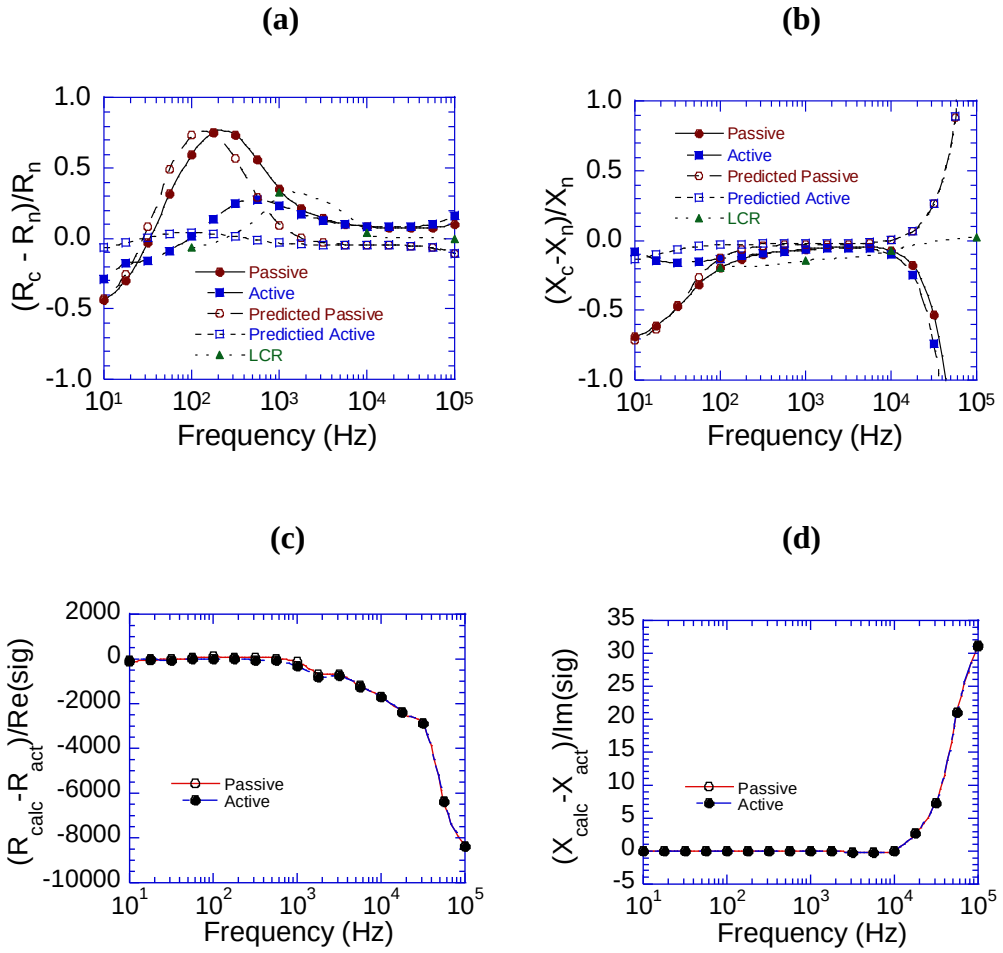
(a)
(b)
(c)
(d)
(Rc - Rn)/Rn
(Xc-Xn)/Xn
(Rcalc-Ract)/Re(sig)
(Xcalc-Xact)/Im(sig)
Frequency (Hz)
Passive
Active
Predicted Passive
Predictied Active
LCR

FIGURE 7

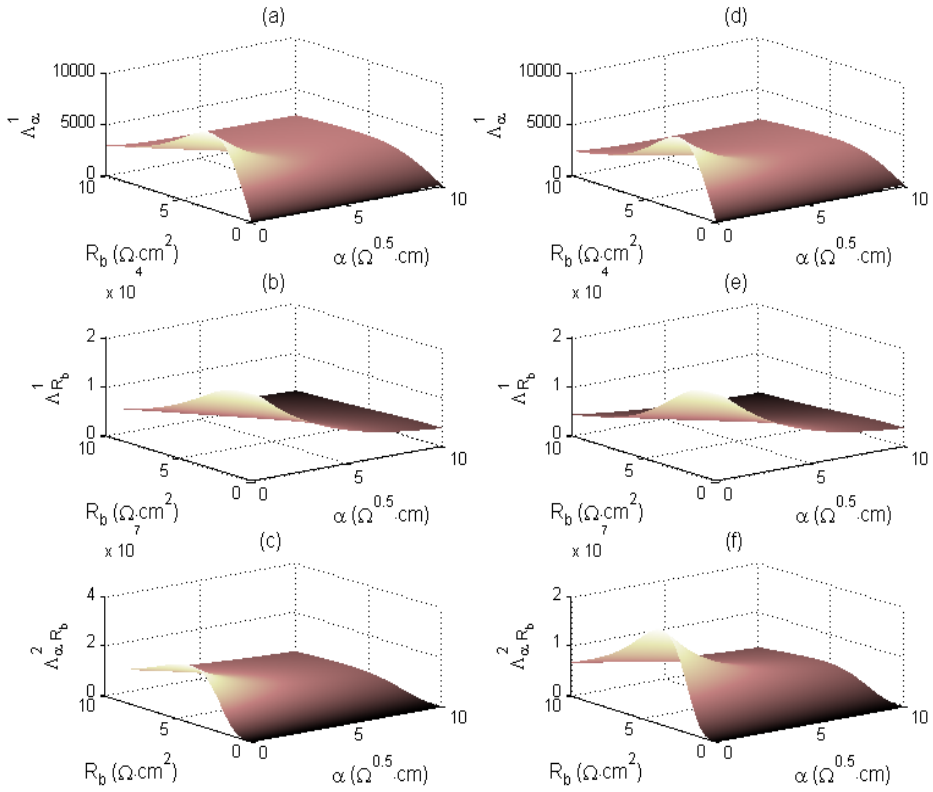
(a)
(b)
(c)
(d)
(e)
(f)
Λ_{α}^{1}
$\Lambda_{R_b}^{1}$
Λ_{α,R_b}^{2}
$R_b\ (\Omega\cdot cm^2)$
$\alpha\ (\Omega^{0.5}\cdot cm)$
x 10^4
x 10^7

FIGURE 8

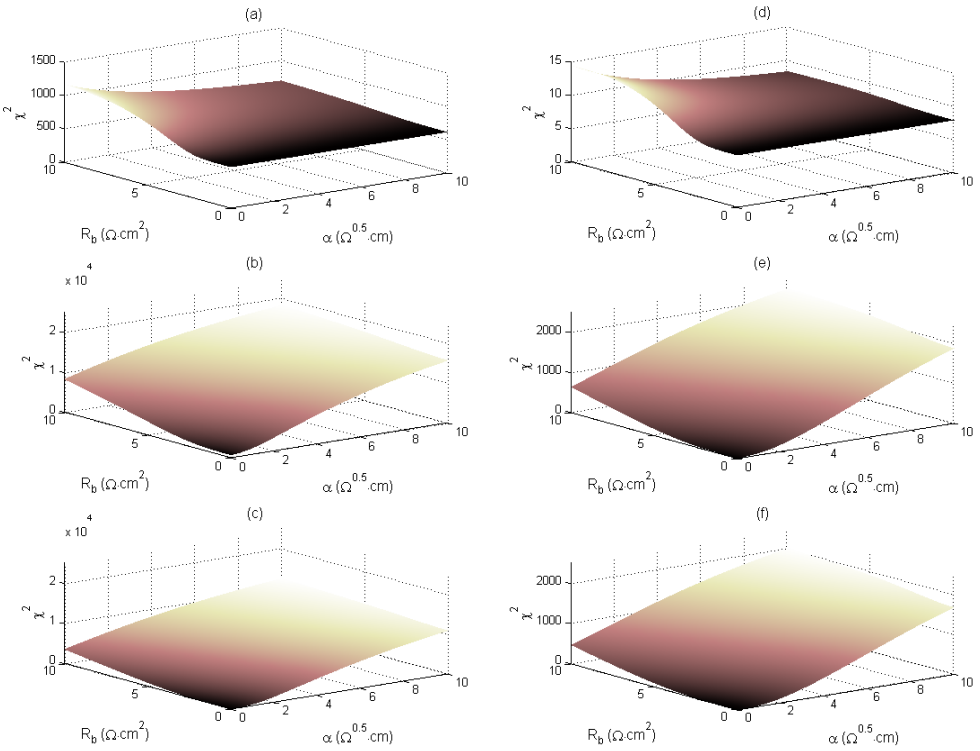

FIGURE 9

(a)

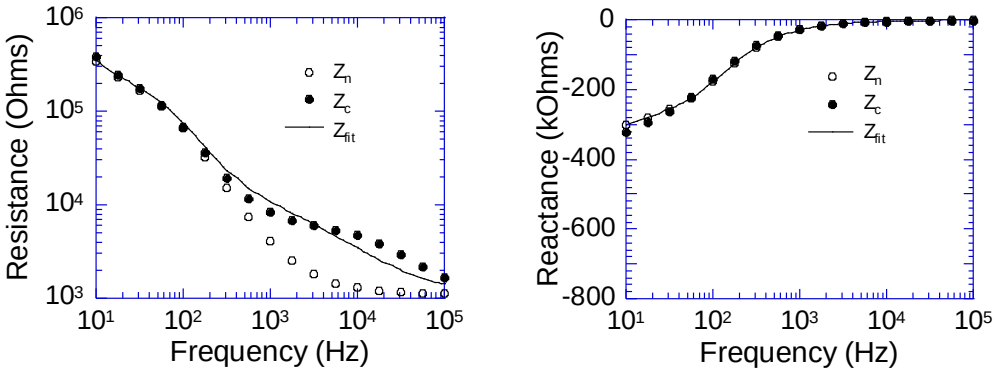
Resistance (Ohms)
Frequency (Hz)
Reactance (kOhms)
Frequency (Hz)
Z_n
Z_c
Z_fit

(b)

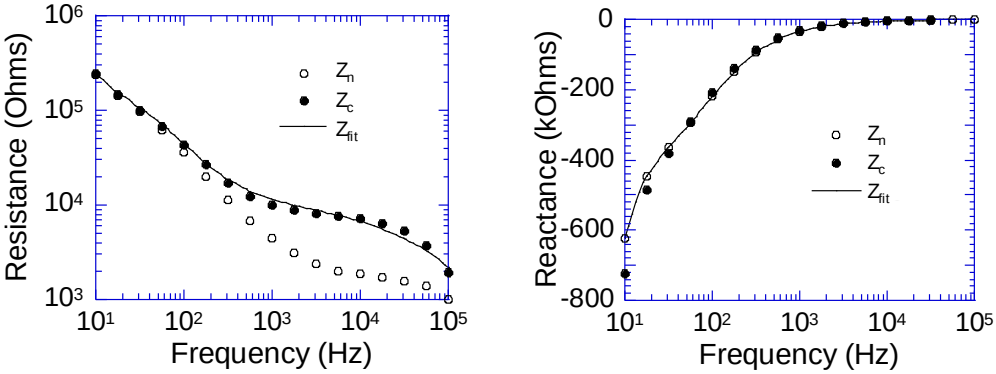
Resistance (Ohms)
Frequency (Hz)
Reactance (kOhms)
Frequency (Hz)
Z_n
Z_c
Z_fit